

Detection of HF and VHF Fields through Floquet Sideband Gaps by ‘Rabi Matching’ Dressed Rydberg Atoms

Andrew P. Rotunno,¹ Samuel Berweger,¹ Nikunj Kumar Prajapati,¹ Matthew T. Simons,¹ Alexandra B. Artusio-Glimpse,¹ Christopher L. Holloway,^{1, a)} Maitreyi Jayaseelan,² R. M. Potvliege,³ and C. S. Adams³

¹⁾*National Institute of Standards and Technology, Boulder, CO 80305, USA*

²⁾*Department of Physics, University of Colorado, Boulder, Colorado 80302, USA*

³⁾*Department of Physics, Durham University, South Road, Durham DH1 3LE, United Kingdom*

(Dated: 25 April 2023)

Radio frequencies in the HF and VHF (3 MHz to 300 MHz) bands are challenging for Rydberg atom-based detection schemes, as resonant detection requires exciting the atoms to extremely high energy states. We demonstrate a method for detecting and measuring radio frequency (RF) carriers in the HF and VHF bands via a controlled Autler-Townes line splitting. Using a resonant, high-frequency (GHz) RF field, the absorption signal from Townes-Meritt sidebands created by a low frequency, non-resonant RF field can be enhanced. Notably, this technique uses a measurement of the optical frequency separation of an avoided crossing to determine the amplitude of a non-resonant, low frequency RF field. This technique also provides frequency-selective measurements of low frequency RF electric fields. To show this, we demonstrate amplitude modulated signal transduction on a low frequency VHF carrier. We further demonstrate reception of multiple tones simultaneously, creating a Rydberg ‘spectrum analyzer’ over the VHF range.

I. INTRODUCTION

Highly excited Rydberg atomic states^{1,2} have been used as self-calibrated sensors for both dc^{3–5} and resonant radio frequency (RF)^{6–9} electric fields, due to the large dc polarizability of the higher orbital angular momentum states^{10,11} and the large transition dipole moments of transitions between nearby Rydberg states. Atomic energy levels are typically probed spectroscopically via electromagnetically-induced transparency (EIT). RF and dc electric fields are measured by changes in the EIT spectrum, with values and uncertainties based on physical atomic quantities. Measurements of laser transmittance alone are subject to many experimental sources of noise, but frequency-space measurements of atomic states using a scanning laser provide a more robust measurement.

Autler-Townes (AT) splitting caused by resonant RF fields provides measurement of GHz to THz fields, traceable to the International System of Units (SI)¹², often with excellent accuracy. One advantage to using Rydberg atoms for RF field sensing is their broad frequency range of operation. This is enabled by the spectral density of Rydberg states, with many large electric dipole moment transitions with resonant frequencies from MHz to THz. However, Rydberg transitions in the HF and VHF range of 3 MHz to 300 MHz require either very high principal quantum number states ($n > 100$), or high orbital angular momentum states^{13,14}. Either method suffers from weaker optical couplings for EIT, as well as contamination of the signal from the very large density of nearby atomic states. Off-resonant generalized Rabi measurements are possible using nearby existing resonances¹⁵, or

farther away using ac Stark shifts with a strong local oscillator (LO)¹⁶. A dc field can also be used to shift the resonance, though this may require a very strong and spatially homogeneous dc field. Power and frequency tuning methods^{17–19} exist for shifting resonances to meet an arbitrary field, but these require signals near existing resonances. The ability to detect low frequency or long-wavelength signals would enable long-distance reception in a compact form factor, with the active receiver volume only a few cm³, compared to meters or longer classical dipole antennas^{9,20,21}, enabling compact long-distance reception for over-the-horizon, underground, or underwater applications.

Here we present a method for the detection of arbitrary electric fields in the 3 MHz to 300 MHz range (we will henceforth use HF and VHF interchangeably for the purpose of this paper) using a Rydberg state with no nearby HF or VHF transitions. We use a high-frequency RF field that is resonant with a nearby Rydberg transition to ‘match’ the Rabi frequency with an applied HF signal field. Tuning the Rabi frequency of the ‘matching’ field effectively probes the Floquet sideband structure generated by the HF field. Absorption dips within the AT peaks reveal an avoided energy crossing, at the mid-point of the Floquet quasi-energy sidebands and the central EIT line. The generation of the Floquet sidebands can be referred to as the Townes-Meritt (TM) effect^{22–25}, where cyclic modulation of state’s Stark shift energy with a MHz-range field will produce quasi-energy sidebands on the observed EIT line^{26–31}. This effect has been analyzed in other quantum systems as well as Rydberg EIT^{32–34}.

To probe the TM or ‘Floquet’ sidebands caused by an HF field, we drive a simultaneous AT splitting, which splits both the center EIT peak and the sidebands. When we ‘match’ the dressing field’s Rabi frequency to the ap-

^{a)}christopher.holloway@nist.gov

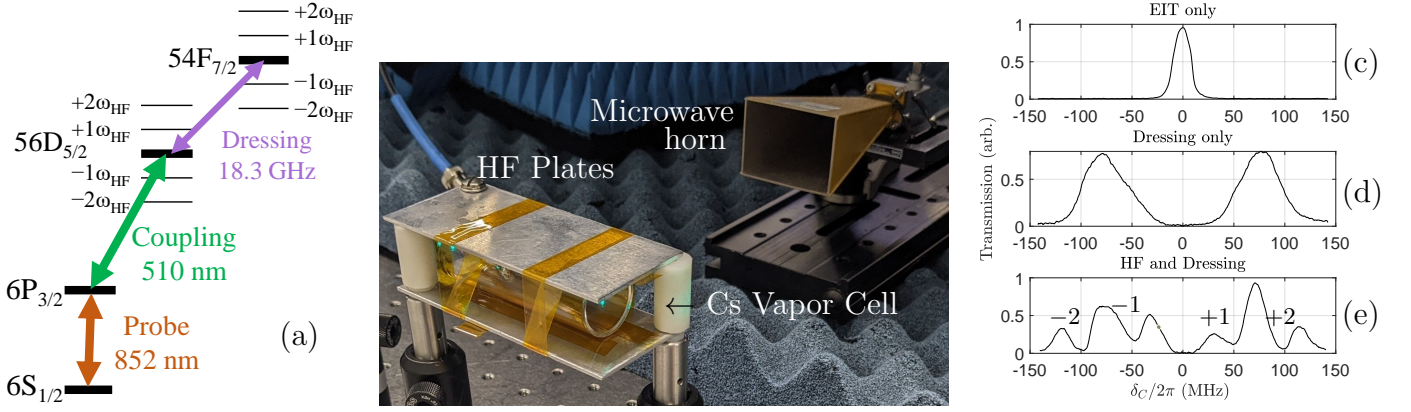


FIG. 1. Overview of the experiment. (a) Atomic level diagram, (b) Experimental setup, and sample transmittance curves comparing (c) unperturbed EIT, (d) the dressed AT splitting with $\Omega_{dr} \approx 2\pi \times 150$ MHz, and (e) with the HF field ($E_{HF} \approx 0.14$ V/cm) at 100 MHz (blue). The two pairs of observed line splittings are labelled ± 1 and ± 2 . The Stark offset has been removed for illustration.

plied HF, an avoided level crossing between the splitting EIT line and its sidebands is observed. The frequency gap grows non-linearly with the HF field strength. We briefly illustrate the effect in Fig. 1, showing (a) an atomic energy level diagram, and (b) the experimental setup, and in (c-e) we show transmittance spectra demonstrating the effect of a 100 MHz HF field on microwave-driven EIT-AT spectrum. We observe both first and second order sidebands in transmittance signal at ± 50 MHz and ± 100 MHz detuning from the central EIT line. With appropriate atomic analysis, the non-linear HF field splitting gives measurements of electric field ac amplitude and dc offset³⁵, as well as the frequency via the spectrum, and phase can be measured with an LO. The splitting allows for a measurement range continuous from a low end of the EIT Doppler linewidth to an upper roll-off with broadening caused by field non-uniformity³⁶, roughly 5 MHz to 500 MHz in our demonstration. In principle, the range can be extended up to GHz with uniform electric fields, and sub-MHz with Doppler cancellation or cold atoms.

We discuss our experimental setup in Sec. II, and present a combination of Floquet and dressed atom theory in Sec. III and Appx. A. We show results of experimental data against theory and the effect of multiple simultaneous HF fields in Sec. IV. Looking toward applications, we demonstrate the ability to perform ‘pseudo-resonant’ HF detection in Sec. VB, and conclude in Sec. VI. In Appx. C, we list the non-standard symbols used in this paper.

II. EXPERIMENTAL SETUP

The Rydberg EIT-AT setup is shown in the level diagram of Fig. 1(a) and image of the experiment Fig. 1(b), including two counter-propagating lasers, a cesium vapor cell (75 mm \times 25.4 mm \varnothing) between two parallel plates, and a K-band microwave horn placed approximately

15 cm from the atoms. The 852 nm probe laser is held near resonance on the D2 transition $|6S_{1/2}, F=4\rangle \leftrightarrow |6P_{3/2}, F=5\rangle$. The probe transmittance is measured through differential detection, with and without the overlapping 510 nm coupling laser. The coupling laser frequency detuning δ_C from the $|56D_{5/2}\rangle$ state EIT resonance is scanned for an EIT spectrum measurement. The probe beam had a $(1/e^2)$ waist diameter of 1.03 mm and a power of 0.5 mW, yielding a probe Rabi frequency of $\approx 2\pi \times 31.5$ MHz. The coupling beam had a waist diameter of 1.7 mm and a power of 33 mW, yielding a coupling Rabi frequency of $\approx 2\pi \times 0.9$ MHz³⁷. In this letter we plot the differential probe transmittance intensity as a false-color axis while coupling laser detuning $\delta_C/2\pi$ is scanned on the horizontal axis, averaged over 5 traces in the oscilloscope before read-out. Scanning either HF or RF power along the vertical axis gives ‘waterfall’ spectrum plots of experimental data that we compare against theory. Long-term drifting offsets of the coupling laser are corrected using a simultaneous field-free reference cell, and the frequency scale is given by the low-field limit of the fine energy gap between the $|56D_{3/2}\rangle$ and $|56D_{5/2}\rangle$ states (392 MHz³⁷).

The resonant GHz dressing field is applied using a horn antenna, also shown in Fig. 1(b). Given the long wavelength of the HF and VHF bands, instead of using a large antenna for propagation, we apply these RF fields across two parallel plates (shown in Fig. 1(b))^{27–31,38}. Each plate is 102 mm \times 45 mm in size, supplied electrically by stranded wires screwed down at tapped holes near the corner, and separated by two 25.4 mm insulating dowels on opposite corners. While the impedance of the glass cell is unknown at low frequency, in theory the glass vapor cell insulates against external dc-limit electric fields³⁹. However, we observe a residual dc or root-mean-squared (RMS) electric field in the following atomic measurements, possibly due to internal residual or laser-induced charges²⁶, or background radio waves.

The Rydberg transition driven by the dressing field is illustrated in Fig. 1(a), on $|56D_{5/2}, m_J = \frac{1}{2}\rangle \leftrightarrow |54F_{7/2}, m_J = \frac{1}{2}\rangle$, which has a dipole transition strength of $1746\ e a_0$, and transition frequency measured near 18.313(1) GHz, significantly different than the expected resonance at 18.346 GHz³⁷, indicating a potential stray field in the cell. This applied frequency ω_{dr} must compensate for the differential Stark shifting of both states with the HF power, P_{HF} . This effective resonance is determined by hand-tuning ω_{dr} at MHz intervals to obtain equal AT peaks in the low-field limit, then the high-field limit when the HF is applied. This shift was measured empirically at roughly $-579(14)$ MHz per mW applied at 100 MHz, and using the power-to-field conversion determined in Sec. IV, nearly $-3.62(9)$ GHz per $(\text{V/cm})^2$, about 4% below the theory value from the difference in polarizabilities (see Appx. A). This power conversion ($\sqrt{P_{HF}}$ to $|E_{HF}|$) is measured at 100 MHz, and in general depends on the frequency-dependent coupling of the plates and vapor cell. In order to make this conversion, we require an atomic theory for the measurement of E_{HF} using the observed splittings.

III. THEORY

We employ a model where the Rabi frequency Ω_{dr} of the dressing field drives resonant transitions between two Floquet ‘ladders’ of quasi-energy states, as illustrated in Fig. 1(a). We differentiate the method used here, namely the Floquet expansion of a dressed two-level system, from other methods including the use of a modulated RF field^{40–45}, multiple tones near Rydberg resonances^{46–52}, leverage off-resonant ac Stark tuning using a resonance^{43,53}, use continuous resonance tuning methods^{17,18}, or observe Floquet (TM) sidebands alone^{22,26–28,54}. Analysis for two-level physics where the states are dressed and driven have been performed^{33,34,55,56}, and the effect can be extended to other driven two-level quantum systems.

We focus on the dynamics of a two-state Rydberg system, leaving aside details of the two-photon cascade EIT which populates Rydberg states and probes energy levels spectrally⁴. We consider the states $|56D_{5/2}, m_J = \frac{1}{2}\rangle = |D\rangle$ and $|54F_{7/2}, m_J = \frac{1}{2}\rangle = |F\rangle$ in Cesium, which are subject to three relevant electric fields at different rates, simultaneously, applied perpendicular to the table: 1) the dressing field is nearly resonant to the strong D-F Rydberg transition $\omega_{dr} \simeq \omega_F - \omega_D$, performing controlled AT splitting, 2) an HF field of interest at a much lower frequency $\omega_{HF} \ll \omega_F - \omega_D$ which populates Floquet sidebands in the EIT spectrum, and 3) a dc or off-resonant effective RMS background field which exists in the cell.

In the low-field limit, the Stark energy shift due to the HF field evolves over time as $-\alpha_{D/F}\mathcal{E}(t)^2/2$, proportional to electric field squared $\mathcal{E}(t)^2$, and dc polarizabilities $\alpha_{D/F}$, where the subscript $(\cdot)_{D/F}$ represents

throughout the value for either individual state. Proper Stark shift calculations are required at higher fields, considering contributions from many allowed dipole transitions which couple to the electric field, contributing to total energy shift and population mixing. We show polarizability calculations for $|D\rangle$ and $|F\rangle$ in Appx. B. We fit frequency shift over \mathcal{E}^2 for effective polarizability in the field range used in this work. Throughout this analysis we use $\alpha_D = -3003$ MHz per $(\text{V/cm})^2$ and $\alpha_F = 12100$ MHz per $(\text{V/cm})^2$. We utilize an effective polarizability for its computational simplicity, although one could use a ‘multi-state’ computation using relevant states from the Stark calculation for more accuracy, especially for high fields. For instance, the $|F\rangle$ state represents $< 90\%$ of the population for only $0.008 (\text{V/cm})^2$, shown in Appx. B. We see good agreement between a multi-state model and the one employed here over the modest field ranges used, and we plan to investigate features which are only captured by a multi-state model in future work.

The electric field of our HF sinusoid and a dc offset can be written $\mathcal{E}(t) = E_{dc} + E_{HF} \cos(\omega_{HF}t)$. The E_{dc} term can be considered to contain broadband background ac electric fields, effectively an RMS contribution to the average dc field value. Since the Stark shift $-\alpha_{D/F}|\mathcal{E}(t)|^2/2\hbar$ is proportional to field squared, we use the following abbreviations for the ac (\sim), dc ($-$), and cross-term (\times) components:

$$\begin{aligned}\Sigma_{D/F}^{\sim} &= \frac{-\alpha_{D/F}E_{HF}^2}{4\hbar} \\ \Sigma_{D/F}^{-} &= \frac{-\alpha_{D/F}E_{dc}^2}{2\hbar} \\ \Sigma_{D/F}^{\times} &= \frac{-\alpha_{D/F}E_{dc}E_{HF}}{\hbar}\end{aligned}\quad (1)$$

letting us write the time-evolving Stark shifts:

$$\begin{aligned}\frac{-\alpha_{D/F}|\mathcal{E}(t)|^2}{2\hbar} &= \Sigma_{D/F}^{-} + \Sigma_{D/F}^{\sim} \\ &+ \Sigma_{D/F}^{\times} (e^{i\omega_{HF}t} + e^{-i\omega_{HF}t})/2 \\ &+ \Sigma_{D/F}^{\sim} (e^{i2\omega_{HF}t} + e^{-i2\omega_{HF}t})/2\end{aligned}\quad (2)$$

When time-averaging, only the first two terms remain, the dc and HF RMS fields, which define our time-averaged shifted resonance from $\omega_{dr} \simeq \omega_F - \omega_D$. That is, due to a differential Stark shift from the HF field intensity, an applied dressing field must shift in order to observe equal AT splitting of the EIT line, with a new effective detuning between the applied field ω_{dr} and the shifted resonance: $\delta_{dr} \equiv \omega_{dr} - [(\omega_F + \Sigma_F^{-} + \Sigma_F^{\sim}) - (\omega_D + \Sigma_D^{-} + \Sigma_D^{\sim})]$. We adjust the applied value of ω_{dr} to keep $\delta_{dr} \simeq 0$ in the high-field limit, by optimizing the symmetry of spectral peaks. We also invoke a detuning scaling parameter to compensate for the difference in experimental resonance shift and the theory values from the effective polarizabilities: $\omega_{dr} - (\omega_F - \omega_D) = S_\delta \cdot (\Sigma_F^{-} + \Sigma_F^{\sim} - \Sigma_D^{-} - \Sigma_D^{\sim})$, where the scaling parameter $S_\delta = 1$ gives the theoretical resonance ($\delta_{dr} = 0$).

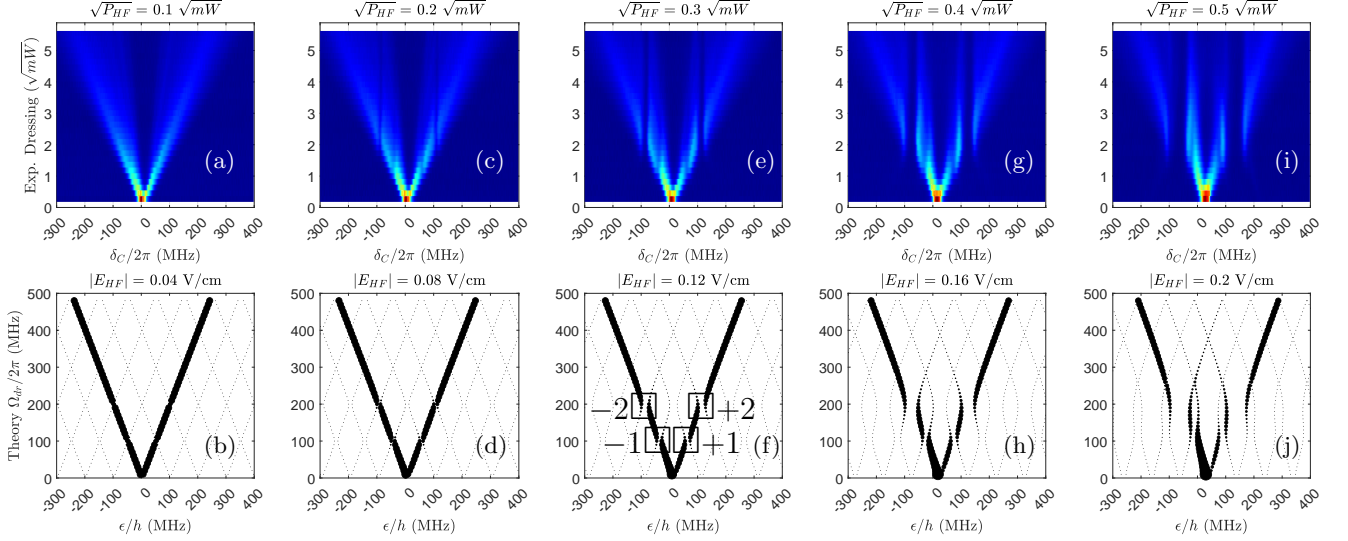


FIG. 2. Comparison of experiment and theory, with the two pairs of avoided crossings labelled $\pm 1, \pm 2$. Top: Experimentally observed transmittance spectra showing a waterfall over applied dressing field vertically, with each plot from left to right increasing amplitude ($\sqrt{P_{HF}}$) of a 100 MHz HF field. Bottom: Calculated state quasi-energy ε , with state projection of $|56D_{5/2}\rangle$ as marker size, plotted as a corresponding waterfall over Ω_{dr} . Theory plots use $E_{dc} = 0.02$ V/cm, $N_{max} = 24$, $S_\delta = 1.1$, scaling $\Omega_{dr}/\sqrt{P_{dr}} = 85 \times 2\pi$ MHz/ \sqrt{mW} , varying Ω_{dr} and E_{HF} as labeled.

Aside from constant terms, there are oscillating components: a dc-inclusive cross term at $\pm 1\omega_{HF}$ with strength $\Sigma_{D/F}^x/2 \propto E_{dc}E_{HF}$, and an ac ‘intensity’ term at $\pm 2\omega_{HF}$ with strength $\Sigma_{D/F}^{\sim}/2 \propto E_{HF}^2$. The rectified oscillating field $\cos^2(\phi) = \frac{1}{2}(1 + \cos(2\phi))$ doubles the effective modulation frequency, making even quasi-energy sidebands with multiples of $2\omega_{HF}$ from the center EIT line³¹. The dc field breaks this symmetry, enabling single ω_{HF} photon transitions, thus odd sidebands in multiples of ω_{HF} ²⁷. For the case of two applied HF frequencies, we expect ac components which oscillate at sum and difference frequencies as $\cos(\phi)\cos(\theta) = \frac{1}{2}[\cos(\phi - \theta) + \cos(\phi + \theta)]$, which are demonstrated in Sec. IV.

We discuss the creation of a time-independent Hamiltonian using both Floquet states and the dressed-atom approach in Appendix A. Diagonalizing this Hamiltonian reveals an overall energy structure where states populate a ‘split ladder’ of states with eigen-energies $\varepsilon_{N,\pm} \approx N\hbar\omega_{HF} \pm \hbar\Omega_{dr}/2$ around the original state energy $\varepsilon_0 \approx \Sigma_D^- + \Sigma_D^+$, for integer N . That is, on either side of the EIT resonance ε_0 , we observe a first order pair of sidebands $\varepsilon_{\pm 1}$ at $\varepsilon_0 \pm \omega_{HF}$, a second order pair $\varepsilon_{\pm 2}$ at $\varepsilon_0 \pm 2\omega_{HF}$, and so on. Each quasi-energy ladder state splits into the (\pm) AT dressed states $\varepsilon_{N,\pm}$, approximately separated by Rabi frequency $\Omega_{dr} = \wp_{DF}E_{dr}/\hbar$ with dipole moment $\wp_{DF} = \langle D | e \cdot \hat{z} | F \rangle$, as shown in Fig. 2(a,b). However, when these splitting sidebands approach each other (moving up the waterfall plot from the bottom), we observe an avoided energy level crossing which alters the state energies, and depends on both the HF and dressing fields, as seen in Fig. 2(c-j) over in-

creasing E_{HF} . We find that the observed effect cannot be interpreted as a simple linear second splitting of the dressed Rydberg states, due to the apparent non-linear splitting by the HF field, and the appearance of two pairs of HF resonances.

The characteristic feature of this method is observed as two pairs of avoided energy crossings in the spectrum for $\Omega_{dr} \simeq \omega_{HF}$ and $\Omega_{dr} \simeq 2\omega_{HF}$ in the presence of an HF field ω_{HF} . The case of $\Omega_{dr} \simeq \omega_{HF}$ we refer to as the ± 1 feature (or $\varepsilon_{0,\pm} \simeq \varepsilon_{\pm 1,\mp}$), and the case of $\Omega_{dr} \simeq 2\omega_{HF}$ we call the ± 2 feature (or $\varepsilon_{0,\pm} \simeq \varepsilon_{\pm 2,\mp}$). These splittings grow non-linearly with $\Sigma_{D/F}^x/\omega_{HF}$ and $\Sigma_{D/F}^{\sim}/\omega_{HF}$, respectively. The spectral location of the avoided level crossing in the resonant case $\delta_{dr} = 0$ (leaving aside the shift of $\Sigma_D^- + \Sigma_D^+$) is at $\pm\omega_{HF}/2$ for the first crossing and $\pm\omega_{HF}$ for the second crossing. These are at the mid-points between ε_0 and $\varepsilon_{\pm 1}$, and ε_0 and $\varepsilon_{\pm 2}$, respectively.

To explain these additional avoided level crossings, we find that we can identify allowed transitions by considering the parity of the states involved and counting photons. The $\pm 1\omega_{HF}$ modulation drives an allowed transition between adjacent Floquet states of opposite (odd) parity, similarly for the $\pm 2\omega_{HF}$ modulation allows a transition to the same (even) parity sideband. We note only the first and second order sideband crossings with the center ε_0 state are strongly avoided, while higher order crossings (> 2) do not have a significant gap.

Deriving a closed-form expression for field values from a splitting measurement remains non-trivial, (i.e. not linear with field as in AT splitting), as the combination of both dressing and HF fields shift the avoid energy crossings, and effective state polarizability depends on the

range of E_{HF} . This leaves us to diagonalize the Hamiltonian in Eq. A5 to find eigen-energies for various field values, and compare those to experimental field waterfall spectra, as in Sec. IV. We did not attempt to calculate theory transmittance spectrum curves, although proper fitting would require this, and such theory could incorporate the range of Rabi frequencies sampled and Doppler effects, but is computationally expensive.

IV. RESULTS

The primary finding here is the ability to detect far off-resonant HF and VHF signals using an induced line splitting, in order to convert a relative transmittance measurement to a more accurate frequency-space measurement. With control over laser detuning δ_C and dressing strength Ω_{dr} , we can measure an arbitrary HF field's frequency, dc and ac components in a single spectrum. This provides a path to atomic measurements of field amplitudes over decades of frequency range (3 MHz to 300 MHz here), with around one decade of dynamic range demonstrated here. A sample measurement is shown in Fig. 1, where transmittance spectra versus coupling laser detuning show (c) Rydberg EIT, (d) resonant dressing AT splitting, and (e) two pairs of absorption features, labelled ± 1 and ± 2 . Spectra like Fig. 1(e) for different RF powers are combined to create waterfall plots in following figures.

In Fig. 2, we compare experimental waterfalls over AT splitting Ω_{dr} via controlled microwave power (top row), with calculated state quasi-energies (bottom row), illustrating the ' ± 1 ' ($\Omega_{dr} \approx \omega_{HF}$) and ' ± 2 ' ($\Omega_{dr} \approx 2\omega_{HF}$) pairs of splittings. We vary P_{HF} so that E_{HF} changes linearly between columns, then adjust ω_{dr} so that $\delta_{dr} \simeq 0$ in the high Ω_{dr} limit. We use the overlay theory points on transmittance data to 'fit-by-eye' to determine an input power to applied field conversion for the HF, the background field E_{dc} , and the dressing power-to-Rabi frequency conversion. Comparing theory to experiment yields an input power to applied field calibration factor C_{PF} ($\sqrt{P_{HF}} = C_{PF}|E_{HF}|$) conversion at 100 MHz of $C_{PF} \approx 0.40$ V/cm per $\sqrt{\text{mW}}$. Due to the frequency-dependent coupling of the plates and the glass cell, we expect this conversion to change across applied ω_{HF} . We estimate a conservative error of order 10%, given a combination of non-linear polarizability effects, EIT linewidth, and non-uniformity of Ω_{dr} . Additionally, the existence of a ± 1 sideband suggests residual dc field in the cell, estimated at around $E_{dc} = 20$ mV/cm, using the size of the ± 1 splittings as E_{HF} varies. We also use this method to obtain the Rabi frequency conversion of $\Omega_{dr} \approx 2\pi \times 85$ MHz per $\sqrt{\text{mW}}$ of dressing power P_{dr} , using the low-field limit of HF in Fig. 2(a,b).

In Fig. 3, we show spectra in waterfalls over E_{HF} with fixed Ω_{dr} , showing the non-linear induced splitting within each AT peak, as well as the Stark shifting of the $|D\rangle$ state with E_{HF}^2 . Experimentally, Ω_{dr} is

held constant ($\approx \omega_{HF}$ or $2\omega_{HF}$), but ω_{dr} is varied to maintain $\delta_{dr} \simeq 0$ between rows. We do not compensate for frequency-dependent horn gain as we maintain signal generator output power across frequencies. The comparison of theory with experiment shows characteristic agreement, which we expect to break down over the higher field values employed, as the real state energy shifts differ from the quadratic polarizability model employed. The broadened lines in experimental AT spectra represent a sample over many values of a spatially non-uniform Ω_{dr} strength, while theory assumes a single value of Ω_{dr} . As well, a constant $\alpha_{D/F}$ is employed over all sets, but in general this depends on E_{HF} amplitude. There is significant interplay in the level shifts due to both fields at high power, causing difficulty in accurate modeling with simple two-level approximations, or obtaining closed-form expressions for the gap. Nevertheless, this measurement demonstrates a path toward making a spectral measurement of E_{HF} and E_{dc} , using a controlled microwave dressing field.

V. APPLICATIONS

We demonstrate two applications for HF field detection using the approach presented here. The first example demonstrates the ability to detect multiple low frequencies fields and the second example demonstrate the detection of a amplitude modulation (AM) of a HF carrier.

A. Multiple Signal Detection

First, we demonstrate ability to detect multiple HF field simultaneously, and the transmitted spectra for multiple simultaneous HF fields are shown Fig. 4. This figure shows the spectra averaged over many values of Ω_{dr} (as if collapsing the plots of Fig. 2 vertically). We compare (a) no HF field, (b) a 90 MHz, and (c) a 130 MHz field separately, then (d) both simultaneously. For illustration, we subtract the Stark shift so the avoided crossings are symmetric around zero. Notably, we observe Floquet states at the sum and difference frequencies, which then appear as absorption dips, noticeably stronger than either single signal.

B. HF Carrier AM Detection

The ability to continuously measure amplitude of an HF carrier via a laser power transmittance allows for real-time, down-converted reception of amplitude modulated (AM) signals. Notably, this cm-sized atom sensor package is capable of simultaneous reception of meters-long wavelength carriers and microwave frequencies. To demonstrate AM reception (modulating E_{HF}), we apply at 10 kHz AM signal to a varying the ω_{HF} carrier

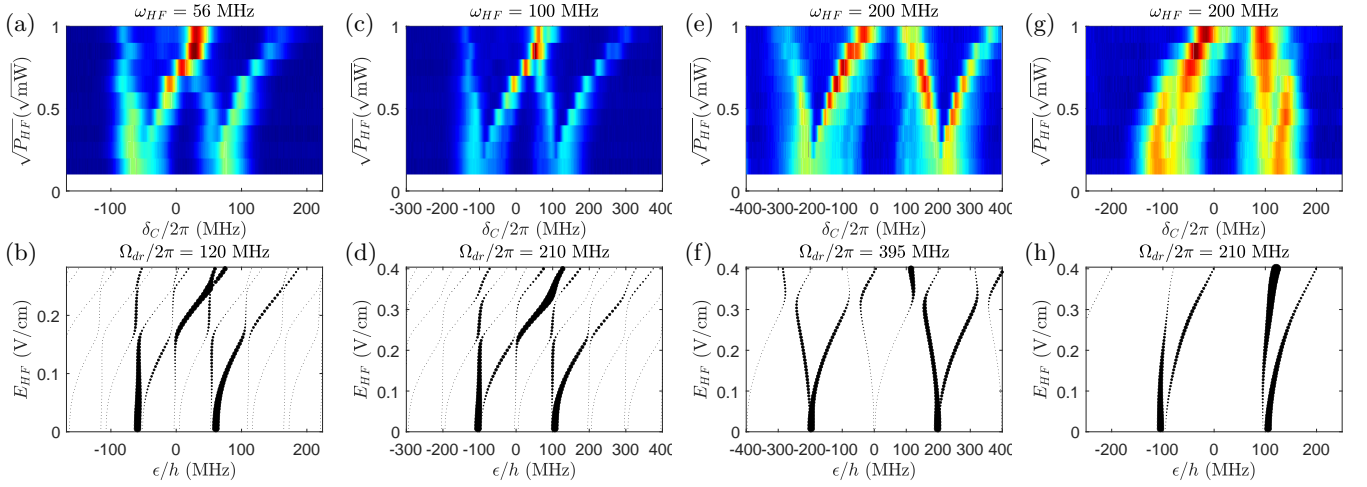


FIG. 3. Effect of increasing HF field, comparing experimental transmittance data (top) with theory quasi-energy (bottom). We show $\omega_{HF} =$ (a,b) 56 MHz, (c,d) 100 MHz, (e-h) 200 MHz, using Ω_{dr} which demonstrate ± 2 (a-f), and ± 1 (g,h) splittings. These plots hold Ω_{dr} constant, keeping experimental $\delta_{dr} \simeq 0$ as E_{HF} grows ($E_{dc} = 20$ mV/cm), using detuning scaling $S_\delta =$ (b) 1.05, (d) 1.1, (f) 0.8, and (h) 0.8.

frequency while Ω_{dr} is providing a significant splitting. We then use a lock-in amplifier on the laser transmittance signal, referenced to the AM signal, while scanning δ_C , tuning lock-in phase to optimize positive peaks. In-phase peaks in the spectrum indicate resonant reception is possible by tuning Ω_{dr} and δ_C . In Fig. 5(a), we show in-phase lock-in amplifier signal as the color axis, across scanning coupling laser frequency, in a waterfall over ω_{HF} , with $\Omega_{dr}/2\pi$ held fixed near 200 MHz. As a result of the induced splitting central to this work, we observe in-phase modulation of the transmittance signal in both AT peaks, when both $\pm 1\omega_{HF}$ and $\pm 2\omega_{HF}$ are brought resonant with Ω_{dr} . We observe signals using only ≈ 20 μ W carrier power, with 50% amplitude modulation, and notably, the Floquet sidebands alone are not visible outside the parts of the spectrum populated by AT peaks. For constant power, the electric field E_{HF} from the plate's impedance depends on ω_{HF} , and we plot $\sqrt{1 - 10^{S_{11}/10}}$, using reflection coefficient of the plates S_{11} in dB, measured by a SNA in Fig. 5(b). We also observe the intensity-based Stark shifting³⁸ of all EIT peaks in the absence of a resonant ω_{HF} carrier, visible in the broad in- and out-of-phase coloring on the right and left sides of each AT peak, around $\delta_C \approx \pm 100$.

In Fig. 5(c), we plot lock-in data slices to simulate the tuned in or ‘pseudo-resonant’ case by fixed laser detuning δ_C (and Ω_{dr}), and scanning ω_{HF} with 5 MHz steps. Resonant peaks in the lock-in data demonstrate the ability to pick out particular carrier frequencies using laser detuning alone. From Fig. 5(c), we can estimate linewidth of order 10 MHz to 20 MHz, using a 5 MHz step size, and this will be the subject of future study.

VI. CONCLUSION

We have demonstrated a method to detect relatively low frequency (3 MHz to 300 MHz) fields using Rydberg states of atoms, by driving AT splitting with Rabi frequency approximately matching the HF frequency, and its second harmonic. The low end of the frequency range is set by EIT linewidth, and the upper end is set by dressing field uniformity. The demonstrated dynamic range is on par with previous TM sideband measurements^{26,27,30}, although could be improved with a LO, or other methods. The observation of a second non-linear splitting due to E_{HF} enables a path to measure field intensity in the HF and VHF range, as well as dc field components, and the frequency of multiple fields simultaneously, from atomic transmittance spectra. While the two-level Floquet theory comparison was able to capture many of the spectral features observed, we expect the precision of this style of field measurement can be improved using a multi-state Stark-shifted approach, especially at higher field values.

Looking toward applications, we demonstrated signal detection on HF carriers, demonstrating its effective band-pass through Rabi matching, which is unavailable to previous Stark-based reception. One apparent limitation of the current apparatus is the non-uniform Ω_{dr} , which will be improved upon in future experiments. As a receiver, this compact cm-sized atomic vapor cell is significantly smaller than wavelength-scale antennas, yet enables a quantum receiver for HF and VHF signals.

Appendix A: Two-level Floquet Theory

When the oscillating HF field modulates state energy faster than the linewidth and away from atomic en-

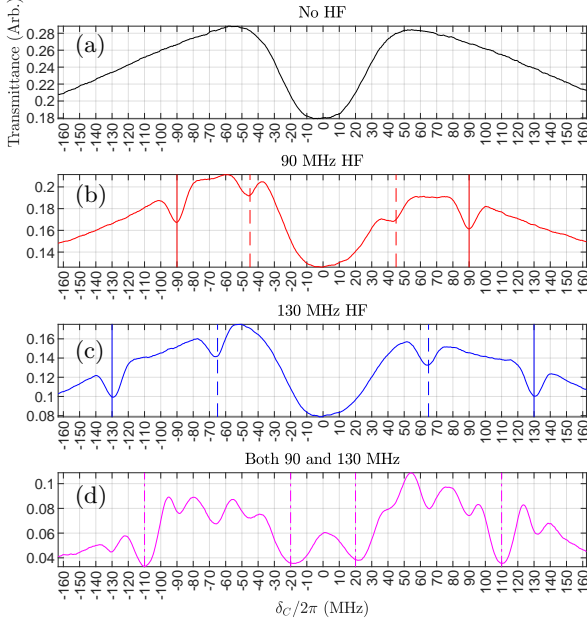


FIG. 4. Demonstration of multiple simultaneous tones. We average spectra over a wide range of Ω_{dr} , and remove the Stark offset. We compare (a) no HF signal, (b) a 90 MHz, (c) 130 MHz HF field, and (d) both fields, each at $P_{HF} = -10$ dBm (≈ 0.14 V/cm at 100 MHz). We denote the ± 2 and the ± 1 absorption features by solid lines and dashed lines, respectively, for the single tones (b,c). When both signals are applied in (d), we denote additional features at half the sum (solid) and difference (dashed) frequencies.

ergy resonances with allowed transitions, one observes induced quasi-energy states at spacing of $\hbar\omega_{HF}$, forming an energy ladder $N\hbar\omega_{HF}$ for integer N . Floquet theory prescribes a method to expand the basis states of a time-dependent Hamiltonian ($i\hbar\frac{dc}{dt} = H(t)c(t)$, where $c(t) = \{d(t), f(t)\}$, the time-evolving state coefficients), into an infinite ladder of states

$$c(t) = \sum_{N=-\infty}^{\infty} c_N \exp(-i\varepsilon_N t/\hbar)$$

Each new basis state has quasi-energy $\varepsilon_N = \varepsilon_0 + N\hbar\omega_{HF}$, relative to the time-average state energies at $\varepsilon_{D/F,0}/\hbar = \omega_{D/F} + \Sigma_{D/F}^- + \Sigma_{D/F}^+$. Population probabilities are calculated by mapping the initial $|d_0|^2 = 1$ state into a new diagonalized basis, and normalizing the resulting eigenvectors. The coefficients of the D and F states' N^{th} sideband are given by d_N and f_N respectively, which are rendered time-independent by this approach. In the absence of a dc field, this 'ladder' of energy states has spacing $2N\omega_{HF}$, as has been observed in Rydberg atoms^{26–31}, well-predicted by this Floquet theory. In the limiting case of $E_{dc} = 0$ and $N \rightarrow \pm\infty$ Floquet states, the height of the N^{th} sideband is given as Bessel functions of order N : $J_N^2\left(\frac{-\alpha E_{HF}^2}{8\omega}\right)$. Calculating a finite Floquet basis re-

quires a truncation of states (from $-N_{max}$ to N_{max} , we use $N_{max} = 24$ throughout) for both the D and F ladders, and for our purposes must include the rf dressing and the dc field.

The time-dependent terms of Eq. 2 will time-average to 0, so we have $\langle \mathcal{E}^2 \rangle = E_{dc}^2 + \frac{E_{HF}^2}{2}$, using the RMS value for the ac part. With this field present, the D and F states shift on average by $\Sigma_D^- + \Sigma_D^+ > 0$, and $\Sigma_F^- + \Sigma_F^+ < 0$. The Stark shift in both states brings the applied dressing frequency ω_{dr} down to the shifted resonance with δ_{dr} (defined in Sec. III) kept near zero as the fields increase. For these states, this differential shifting drops the observed resonance by $(\alpha_D - \alpha_F)/2 = -7.552$ GHz per $(\text{V/cm})^2$.

Applying rf fields nearly resonant to an allowed atomic transition (here, $\omega_{dr} \simeq \omega_F - \omega_D$), one can determine energy levels of the atom-photon-interaction using dressed atom theory. The two-level coupling between the $|D\rangle$ and $|F\rangle$ state has dipole strength $\langle 56D_{5/2}, m_J = \frac{1}{2} | e \cdot \hat{z} | 54F_{5/2}, m_J = \frac{1}{2} \rangle = \wp_{DF} \approx 1746 ea_0 \approx 2234$ MHz per (V/cm) . The time-dependent two-level Hamiltonian is

$$H(t)/\hbar = \begin{pmatrix} \omega_D - \alpha_D \mathcal{E}^2(\omega_{HF}t)/2 + \omega_{dr} & \Omega_{dr} \cos(\omega_{dr}t) \\ \Omega_{dr} \cos(\omega_{dr}t) & \omega_F - \alpha_F \mathcal{E}^2(\omega_{HF}t)/2 \end{pmatrix} \quad (\text{A1})$$

using shorthand $\mathcal{E}^2(\omega_{HF}t) = (E_{dc} + E_{HF} \cos(\omega_{HF}t))^2$. Taking the time-average Stark shifts, we have a well-defined δ_{dr} , and using the rotating wave approximation (RWA) to shortcut another Floquet basis, we write the typical dressed atom Hamiltonian for the two-level atom-photon basis $\{|D, (N_{dr} + 1)\omega_{dr}\rangle, |F, N_{dr}\omega_{dr}\rangle\}$ and setting $\omega_D = 0$:

$$H_{atom-photon} = \hbar \begin{pmatrix} 0 & \Omega_{dr}/2 \\ \Omega_{dr}/2 & -\delta_{dr} \end{pmatrix} \quad (\text{A2})$$

Driving this transition resonantly ($\delta_{dr} = 0$), we induce AT splitting linear with the field applied, given by the Rabi frequency: $\Omega_{dr} = \wp_{DF} E_{dr}/\hbar$. Off resonance, eigen-energies are given by $\varepsilon_{0,\pm} = \frac{\hbar}{2} \left(-\delta_{dr} \pm \sqrt{\delta_{dr}^2 + \Omega_{dr}^2} \right)$ noting that δ_{dr} is defined including time-averaged shifts, and therefore ω_{dr} must shift with P_{HF} to maintain $\delta_{dr} \simeq 0$. The dressing field forms an effective two-level system for each of pair of quasi-energy states, connecting each d_N component to the same N 's f_N state, splitting either state's ε_N quasi-energy into $\varepsilon_{N,\pm}$ dressed state components.

Looking to the time-dependent terms of Eq. 2, we have rotating components at ω_{HF} with strength $\Sigma_{D/F}^\times/2$, the dc mixing term, and at $2\omega_{HF}$ with strength $\Sigma_{D/F}^\sim/2$, the pure ac term. These terms connect Floquet states with $\Delta N = \pm 1$, and $\Delta N = \pm 2$, in addition to the dressing between the d_N and f_N states. We can write the the

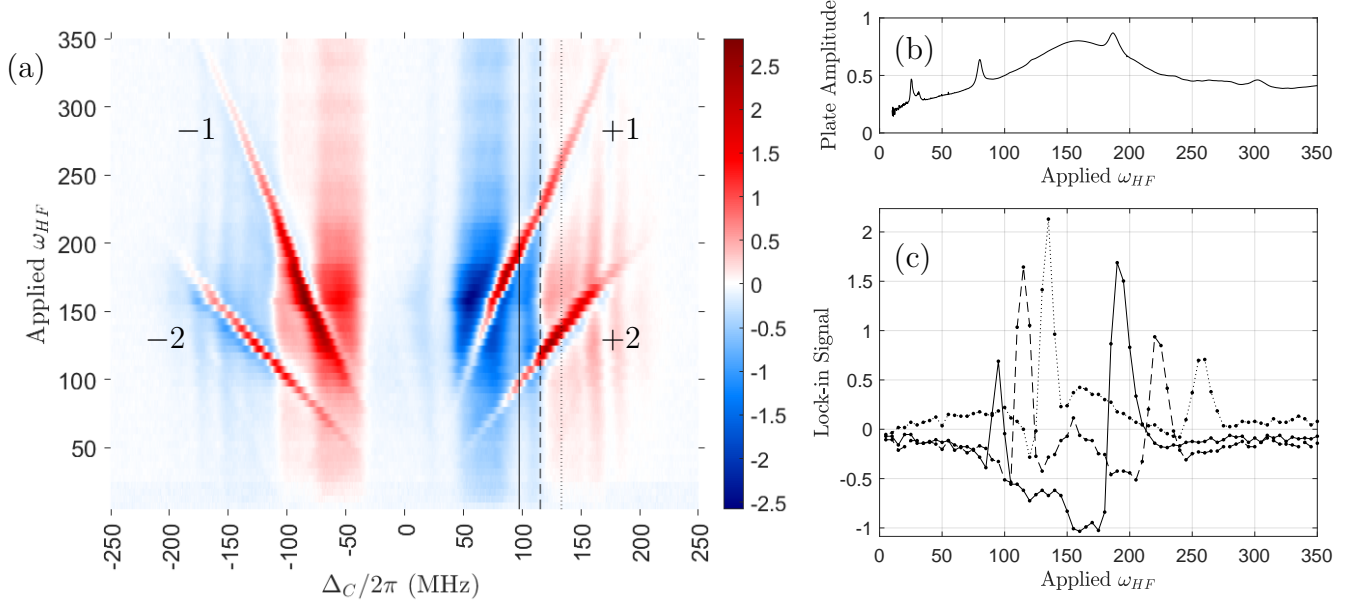


FIG. 5. Detection of AM signals across HF carrier frequency. (a) We plot in-phase lock-in amplifier of the laser transmittance signal referenced to a 10 kHz modulation of P_{HF} , in a waterfall over ω_{HF} , for fixed $\Omega_{dr} \approx 2\pi \cdot 100$ MHz. (b) Expected relative field amplitude from plate impedance measurements (c) Corresponding vertical slices of lock-in signal, as if fixing Δ_C and Ω_{dr}

Schrödinger equation as a system of linear equations:

$$\begin{aligned}
 \varepsilon d_N = & (\Sigma_D^- + \Sigma_D^{\sim} + \omega_{dr} + N\omega_{HF}) d_N \\
 & + \Sigma_D^{\times}/2 (d_{N+1} + d_{N-1}) \\
 & + \Sigma_D^{\sim}/2 (d_{N+2} + d_{N-2}) \\
 & + \Omega_{dr}/2 f_N
 \end{aligned} \tag{A3}$$

and

$$\begin{aligned}
 \varepsilon f_N = & (\Sigma_F^- + \Sigma_F^{\sim} + N\omega_{HF}) f_N \\
 & + \Sigma_F^{\times}/2 (f_{N+1} + f_{N-1}) \\
 & + \Sigma_F^{\sim}/2 (f_{N+2} + f_{N-2}) \\
 & + \Omega_{dr}/2 d_N
 \end{aligned} \tag{A4}$$

The resulting Hamiltonian and basis state vector for this dressed-Floquet system is given in Eq. A5, using $\omega_D + \Sigma_D^- + \Sigma_D^{\sim}$ as the 0 energy reference. The diagonal blocks include on the diagonal the quasi-energy ladder, shifted by time-averaged fields and rendered near-degenerate between diagonal blocks by the addition of $\hbar\omega_{dr}$, included in $\delta_{dr} \simeq 0$. Just off the diagonal, we have the ω_{HF} and $2\omega_{HF}$ interactions between (near-) neighboring quasi-energies. In the off-diagonal blocks, we have the dressing coupling Ω_{dr} between corresponding near-resonant states.

$$\frac{\hat{H}}{\hbar} \left(\frac{d_N \dots}{f_N \dots} \right) = \varepsilon/\hbar \left(\frac{d_N \dots}{f_N \dots} \right) =$$

$\begin{pmatrix} \ddots & \Sigma_D^x/2 & \Sigma_D^y/2 & 0 & 0 & 0 & \ddots \\ \Sigma_D^x/2 & -2\omega_{HF} & \Sigma_D^x/2 & \Sigma_D^y & 0 & 0 & 0 \\ \Sigma_D^y/2 & \Sigma_D^x/2 & -\omega_{HF} & \Sigma_D^x/2 & \Sigma_D^y/2 & 0 & 0 \\ 0 & \Sigma_D^y/2 & \Sigma_D^x/2 & 0 & \Sigma_D^x/2 & \Sigma_D^y/2 & 0 \\ 0 & 0 & \Sigma_D^y/2 & \Sigma_D^x/2 & \omega_{HF} & \Sigma_D^x/2 & \Sigma_D^y/2 \\ 0 & 0 & 0 & \Sigma_D^y/2 & \Sigma_D^x/2 & 2\omega_{HF} & \Sigma_D^x/2 \\ \ddots & 0 & 0 & 0 & \Sigma_D^y/2 & \Sigma_D^x/2 & \ddots \end{pmatrix}$	$\begin{pmatrix} \ddots & 0 & 0 & 0 & 0 & 0 & \ddots \\ 0 & \Omega_{dr}/2 & 0 & 0 & 0 & 0 & 0 \\ 0 & 0 & \Omega_{dr}/2 & 0 & 0 & 0 & 0 \\ 0 & 0 & 0 & \Omega_{dr}/2 & 0 & 0 & 0 \\ 0 & 0 & 0 & 0 & \Omega_{dr}/2 & 0 & 0 \\ 0 & 0 & 0 & 0 & 0 & \Omega_{dr}/2 & 0 \\ \ddots & 0 & 0 & 0 & 0 & 0 & \ddots \end{pmatrix}$	$\begin{pmatrix} \vdots \\ d_{-2} \\ d_{-1} \\ d_0 \\ d_1 \\ d_2 \\ \vdots \end{pmatrix}$
$\begin{pmatrix} \ddots & 0 & 0 & 0 & 0 & 0 & 0 \\ 0 & \Omega_{dr}/2 & 0 & 0 & 0 & 0 & 0 \\ 0 & 0 & \Omega_{dr}/2 & 0 & 0 & 0 & 0 \\ 0 & 0 & 0 & \Omega_{dr}/2 & 0 & 0 & 0 \\ 0 & 0 & 0 & 0 & \Omega_{dr}/2 & 0 & 0 \\ 0 & 0 & 0 & 0 & 0 & \Omega_{dr}/2 & 0 \\ 0 & 0 & 0 & 0 & 0 & 0 & \ddots \end{pmatrix}$	$\begin{pmatrix} \ddots & \Sigma_F^x/2 & \Sigma_F^y/2 & 0 & 0 & 0 & \ddots \\ \Sigma_F^x/2 & -2\omega_{HF} - \delta_{dr} & \Sigma_F^x/2 & \Sigma_F^y & 0 & 0 & 0 \\ \Sigma_F^y/2 & \Sigma_F^x/2 & -\omega_{HF} - \delta_{dr} & \Sigma_F^x/2 & \Sigma_F^y/2 & 0 & 0 \\ 0 & \Sigma_F^y/2 & \Sigma_F^x/2 & -\delta_{dr} & \Sigma_F^x/2 & \Sigma_F^y/2 & 0 \\ 0 & 0 & \Sigma_F^y/2 & \Sigma_F^x/2 & \omega_{HF} - \delta_{dr} & \Sigma_F^x/2 & \Sigma_F^y/2 \\ 0 & 0 & 0 & \Sigma_F^y/2 & \Sigma_F^x/2 & 2\omega_{HF} - \delta_{dr} & \Sigma_F^x/2 \\ \ddots & 0 & 0 & 0 & \Sigma_F^y/2 & \Sigma_F^x/2 & \ddots \end{pmatrix}$	$\begin{pmatrix} \vdots \\ f_{-2} \\ f_{-1} \\ f_0 \\ f_1 \\ f_2 \\ \vdots \end{pmatrix}$

(A5)

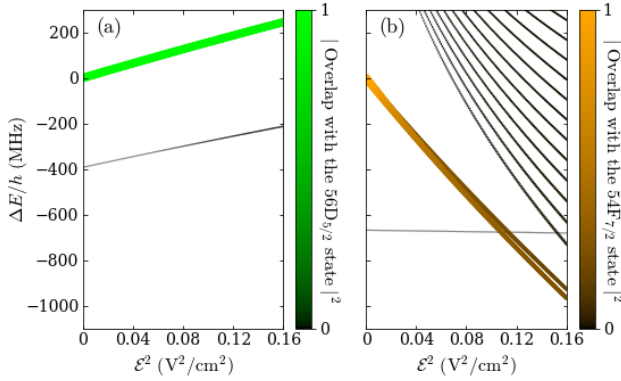


FIG. 6. Results from a many-level calculation of Stark energy shift. Fitting across electric field values gives the effective polarizability used in this paper for $|D\rangle$ in (a), and $|F\rangle$ in (b).

Appendix B: Determining Effective Polarizability

A true Stark energy shift calculation¹⁰ considers coupling to all other atomic states, but in the low field limit, an effective quadratic polarization coefficient is fit from this process. Rather than use the low-field limit for polarizability, we calculate effective polarizabilities in-house, given slightly non-quadratic behavior, for fields up to ≈ 0.4 V/cm. In Fig. 6, we demonstrate an example of calculating the Stark shift from a dc electric field when including all the states which significantly contribute to the energy shift. In principle, this effective polarizability value changes for different maximum fields, which alters the implied measurements of electric field from a spectral gap.

Appendix C: List of Symbols

- ¹T. Gallagher, *Rydberg atoms* (2006).
- ²C. S. Adams, J. D. Pritchard, and J. P. Shaffer, “Rydberg atom quantum technologies,” *Journal of Physics B: Atomic, Molecular and Optical Physics* **53**, 012002 (2019).
- ³A. Osterwalder and F. Merkt, “Using high rydberg states as electric field sensors,” *Physical review letters* **82**, 1831 (1999).
- ⁴A. Mohapatra, T. Jackson, and C. Adams, “Coherent optical detection of highly excited rydberg states using electromagnetically induced transparency,” *Physical review letters* **98**, 113003 (2007).
- ⁵C. L. Holloway, N. Prajapati, J. A. Sherman, A. Rüfenacht, A. B. Artusio-Glimpse, M. T. Simons, A. K. Robinson, D. S. La Mantia, and E. B. Norrgard, “Electromagnetically induced transparency based rydberg-atom sensor for traceable voltage measurements,” *AVS Quantum Science* **4**, 034401 (2022).
- ⁶J. A. Sedlacek, A. Schwettmann, H. Kübler, R. Löw, T. Pfau, and J. P. Shaffer, “Microwave electrometry with rydberg atoms in a vapour cell using bright atomic resonances,” *Nature physics* **8**, 819–824 (2012).
- ⁷C. L. Holloway, J. A. Gordon, A. Schwarzkopf, D. A. Anderson, S. A. Miller, N. Thaicharoen, and G. Raithel, “Sub-wavelength imaging and field mapping via electromagnetically induced transparency and autler-townes splitting in rydberg atoms,” *Applied Physics Letters* **104**, 244102 (2014).
- ⁸A. Artusio-Glimpse, M. T. Simons, N. Prajapati, and C. L. Holloway, “Modern rf measurements with hot atoms: A technology review of rydberg atom-based radio frequency field sensors,” *IEEE Microwave Magazine* **23**, 44–56 (2022).
- ⁹D. H. Meyer, Z. A. Castillo, K. C. Cox, and P. D. Kunz, “Assessment of rydberg atoms for wideband electric field sensing,” *Journal of Physics B: Atomic, Molecular and Optical Physics* **53**, 034001 (2020).
- ¹⁰M. L. Zimmerman, M. G. Littman, M. M. Kash, and D. Kleppner, “Stark structure of the rydberg states of alkali-metal atoms,” *Physical Review A* **20**, 2251 (1979).
- ¹¹Y. Zhang, M. Ciocca, L.-W. He, C. Burkhardt, and J. Leventhal, “Measurement of atomic polarizabilities using floquet spectroscopy,” *Physical Review A* **50**, 1101 (1994).
- ¹²C. L. Holloway, J. A. Gordon, S. Jefferts, A. Schwarzkopf, D. A. Anderson, S. A. Miller, N. Thaicharoen, and G. Raithel, “Broad-band rydberg atom-based electric-field probe for si-traceable,

- self-calibrated measurements,” *IEEE Transactions on Antennas and Propagation* **62**, 6169–6182 (2014).
- ¹³N. Thaicharoen, K. Moore, D. Anderson, R. Powel, E. Peterson, and G. Raithel, “Electromagnetically induced transparency, absorption, and microwave-field sensing in a rb vapor cell with a three-color all-infrared laser system,” *Physical Review A* **100**, 063427 (2019).
 - ¹⁴R. C. Brown, B. Kayim, M. A. Viray, A. R. Perry, B. C. Sawyer, and R. Wyllie, “Vhf/uhf detection using high angular momentum rydberg states,” *arXiv preprint arXiv:2205.12876* (2022), 10.48550/arXiv.2205.12876.
 - ¹⁵M. T. Simons, J. A. Gordon, C. L. Holloway, D. A. Anderson, S. A. Miller, and G. Raithel, “Using frequency detuning to improve the sensitivity of electric field measurements via electromagnetically induced transparency and autler-townes splitting in rydberg atoms,” *Applied Physics Letters* **108**, 174101 (2016).
 - ¹⁶J. Hu, H. Li, R. Song, J. Bai, Y. Jiao, J. Zhao, and S. Jia, “Continuously tunable radio frequency electrometry with rydberg atoms,” *Applied Physics Letters* **121**, 014002 (2022).
 - ¹⁷M. T. Simons, A. B. Artusio-Glimpse, C. L. Holloway, E. Imhof, S. R. Jefferts, R. Wyllie, B. C. Sawyer, and T. G. Walker, “Continuous radio-frequency electric-field detection through adjacent rydberg resonance tuning,” *Physical Review A* **104**, 032824 (2021).
 - ¹⁸S. Berweger, N. Prajapati, A. B. Artusio-Glimpse, A. P. Rotunno, R. Brown, C. L. Holloway, M. T. Simons, E. Imhof, S. R. Jefferts, B. N. Kayim, M. A. Viray, R. Wyllie, B. C. Sawyer, and T. G. Walker, “Rydberg-state engineering: Investigations of tuning schemes for continuous frequency sensing,” *Phys. Rev. Appl.* **19**, 044049 (2023).
 - ¹⁹P. Bohlouli-Zanjani, J. Petrus, and J. Martin, “Enhancement of rydberg atom interactions using ac stark shifts,” *Physical review letters* **98**, 203005 (2007).
 - ²⁰K. C. Cox, D. H. Meyer, F. K. Fatemi, and P. D. Kunz, “Quantum-limited atomic receiver in the electrically small regime,” *Physical Review Letters* **121**, 110502 (2018).
 - ²¹L. W. Bussey, F. A. Burton, K. Bongs, J. Goldwin, and T. Whitley, “Quantum shot noise limit in a rydberg rf receiver compared to thermal noise limit in a conventional receiver,” *IEEE Sensors Letters* (2022), 10.1109/LSENS.2022.3203465.
 - ²²C. Townes and F. Merritt, “Stark effect in high frequency fields,” *Physical Review* **72**, 1266 (1947).
 - ²³W. R. White, “Theoretical study of the townes-merritt effect in level crossing experiments,” Tech. Rep. (FRANK J SEILER RESEARCH LAB UNITED STATES AIR FORCE ACADEMY CO, 1989).
 - ²⁴M. Tanasittikosol, *Rydberg dark states in external fields*, Ph.D. thesis, Durham University (2011).
 - ²⁵S. H. Autler and C. H. Townes, “Stark effect in rapidly varying fields,” *Physical Review* **100**, 703 (1955).
 - ²⁶M. G. Bason, M. Tanasittikosol, A. Sargsyan, A. Mohapatra, D. Sarkisyan, R. Potvliege, and C. Adams, “Enhanced electric field sensitivity of rf-dressed rydberg dark states,” *New Journal of Physics* **12**, 065015 (2010).
 - ²⁷S. A. Miller, D. A. Anderson, and G. Raithel, “Radio-frequency-modulated rydberg states in a vapor cell,” *New Journal of Physics* **18**, 053017 (2016).
 - ²⁸Y. Jiao, X. Han, Z. Yang, J. Li, G. Raithel, J. Zhao, and S. Jia, “Spectroscopy of cesium rydberg atoms in strong radio-frequency fields,” *Physical Review A* **94**, 023832 (2016).
 - ²⁹S. Miller, *Optical Measurements of Strong Radio-Frequency Fields Using Rydberg Atoms*, Ph.D. thesis (2017).
 - ³⁰Y. Jiao, L. Hao, X. Han, S. Bai, G. Raithel, J. Zhao, and S. Jia, “Atom-based radio-frequency field calibration and polarization measurement using cesium n d j floquet states,” *Physical Review Applied* **8**, 014028 (2017).
 - ³¹E. Paradis, G. Raithel, and D. A. Anderson, “Atomic measurements of high-intensity vhf-band radio-frequency fields with a rydberg vapor-cell detector,” *Physical Review A* **100**, 013420 (2019).
 - ³²L. W. Clark, N. Jia, N. Schine, C. Baum, A. Georgakopoulos, and J. Simon, “Interacting floquet polaritons,” *Nature* **571**, 532–536 (2019).
 - ³³S.-K. Son, S. Han, S.-I. Chu, *et al.*, “Floquet formulation for the investigation of multiphoton quantum interference in a superconducting qubit driven by a strong ac field,” *Physical Review A* **79**, 032301 (2009).
 - ³⁴J. Hausinger and M. Grifoni, “Dissipative two-level system under strong ac driving: A combination of floquet and van vleck perturbation theory,” *Physical Review A* **81**, 022117 (2010).
 - ³⁵S. C. y Cruz and B. Mielnik, “The parity phenomenon of the floquet spectra,” *Physics Letters A* **352**, 36–40 (2006).
 - ³⁶A. P. Rotunno, A. K. Robinson, S. Berweger, N. Prajapati, A. B. Artusio-Glimpse, M. Simons, and C. L. Holloway, “Modeling line broadening and distortion due to spatially non-uniform fields in rydberg electrometry,” *arXiv preprint arXiv:2208.07325* (2022), 10.48550/arXiv.2208.07325.
 - ³⁷N. Šibalić, J. D. Pritchard, C. S. Adams, and K. J. Weatherill, “Arc: An open-source library for calculating properties of alkali rydberg atoms,” *Computer Physics Communications* **220**, 319–331 (2017).
 - ³⁸B. Liu, L.-H. Zhang, Z.-K. Liu, Z.-Y. Zhang, Z.-H. Zhu, W. Gao, G.-C. Guo, D.-S. Ding, and B.-S. Shi, “Highly sensitive measurement of a megahertz rf electric field with a rydberg-atom sensor,” *Physical Review Applied* **18**, 014045 (2022).
 - ³⁹Y.-Y. Jau and T. Carter, “Vapor-cell-based atomic electrometry for detection frequencies below 1 khz,” *Physical Review Applied* **13**, 054034 (2020).
 - ⁴⁰D. H. Meyer, K. C. Cox, F. K. Fatemi, and P. D. Kunz, “Digital communication with rydberg atoms and amplitude-modulated microwave fields,” *Applied Physics Letters* **112**, 211108 (2018).
 - ⁴¹D. A. Anderson, R. E. Sapiro, and G. Raithel, “An atomic receiver for am and fm radio communication,” *IEEE Transactions on Antennas and Propagation* **69**, 2455–2462 (2020).
 - ⁴²C. Holloway, M. Simons, A. H. Haddab, J. A. Gordon, D. A. Anderson, G. Raithel, and S. Voran, “A multiple-band rydberg atom-based receiver: Am/fm stereo reception,” *IEEE Antennas and Propagation Magazine* **63**, 63–76 (2020).
 - ⁴³H. Zou, Z. Song, H. Mu, Z. Feng, J. Qu, and Q. Wang, “Atomic receiver by utilizing multiple radio-frequency coupling at rydberg states of rubidium,” *Applied Sciences* **10**, 1346 (2020).
 - ⁴⁴Z.-K. Liu, L.-H. Zhang, B. Liu, Z.-Y. Zhang, G.-C. Guo, D.-S. Ding, and B.-S. Shi, “Deep learning enhanced rydberg multi-frequency microwave recognition,” *Nature communications* **13**, 1–10 (2022).
 - ⁴⁵S. Borówka, U. Pylypenko, M. Mazelanik, and M. Parniak, “Sensitivity of a rydberg-atom receiver to frequency and amplitude modulation of microwaves,” *Applied Optics* **61**, 8806–8812 (2022).
 - ⁴⁶H. Kim, J. R. Park, and H.-W. Lee, “Semiclassical dressed-atom approach,” *Journal of Physics B: Atomic, Molecular and Optical Physics* **33**, 1703 (2000).
 - ⁴⁷D. Anderson, A. Schwarzkopf, S. Miller, N. Thaicharoen, G. Raithel, J. Gordon, and C. Holloway, “Two-photon microwave transitions and strong-field effects in a room-temperature rydberg-atom gas,” *Physical Review A* **90**, 043419 (2014).
 - ⁴⁸D. A. Anderson, S. A. Miller, G. Raithel, J. Gordon, M. Butler, and C. Holloway, “Optical measurements of strong microwave fields with rydberg atoms in a vapor cell,” *Physical Review Applied* **5**, 034003 (2016).
 - ⁴⁹D. A. Anderson and G. Raithel, “Continuous-frequency measurements of high-intensity microwave electric fields with atomic vapor cells,” *Applied Physics Letters* **111**, 053504 (2017).
 - ⁵⁰Y. Xue, Y. Jiao, L. Hao, and J. Zhao, “Microwave two-photon spectroscopy of cesium rydberg atoms,” *Optics Express* **29**, 43827–43835 (2021).
 - ⁵¹Z. Ficek and T. Rudolph, “Quantum interference in a driven two-level atom,” *Physical Review A* **60**, R4245 (1999).
 - ⁵²C. Yu, J. Bochinski, T. Kordich, T. Mossberg, and Z. Ficek, “Driving the driven atom: Spectral signatures,” *Physical Review*

- A **56**, R4381 (1997).
- ⁵³K. Yang, Z. Sun, R. Mao, Y. Lin, Y. Liu, Q. An, and Y. Fu, “Wideband rydberg atom-based receiver for amplitude modulation radio frequency communication,” *Chinese Optics Letters* **20**, 081203 (2022).
- ⁵⁴L. Chai and R. R. Jones, “Demonstration of an rf electrometer based on eit spectroscopy of non-resonantly dressed rydberg atoms,” in *CLEO: Science and Innovations* (Optica Publishing Group, 2021) pp. STu2A–1.
- ⁵⁵M. Tanasittikosol and R. Potvliege, “Sidebands shifts and induced sidebands in rf-dressed rydberg systems,” *arXiv preprint arXiv:1206.5951* (2012), 10.48550/arXiv.1206.5951.
- ⁵⁶J. H. Shirley, “Solution of the schrödinger equation with a hamiltonian periodic in time,” *Physical Review* **138**, B979 (1965).

Symbol	Meaning
EIT	Electromagnetically-Induced Transparency
AT	Autler-Townes effect, dressed state splitting
HF	High Frequency radio band, 3 MHz to 30 MHz
VHF	Very High Frequency radio band, 30 MHz to 300 MHz
TM	Townes-Merritt effect, Floquet quasi-energy sidebands
δ_C	Coupling laser detuning from low-field (reference cell) EIT resonance
ω_{dr}	Dressing field angular frequency
Ω_{dr}	HF field angular frequency
P_{HF}	Power applied to low frequency plates
E_{HF}	Low frequency electric field on plates
E_{dc}	Static electric field inside vapor cell
$\mathcal{E}(t)$	Time-evolving total electric field seen by the atoms
$(\cdot)_{D/F}$	Two values represented, for $56D_{5/2}$ and $54F_{7/2}$
$\hbar\omega_{D/F}$	Energy of the unperturbed $\{D,F\}$ state
$\alpha_{D/F}$	Polarizability of the $\{D,F\}$ state
$\hbar\Sigma_{D/F}^-$	Energy shift from dc + RMS electric field of the $\{D,F\}$ state. See Eq. 1
$\hbar\tilde{\Sigma}_{D/F}$	Energy shift from the HF RMS electric field of the $\{D,F\}$ state. See Eq. 1
$\hbar\Sigma_{D/F}^\times$	Energy shift from ac/dc cross term of the $\{D,F\}$ state. See Eq. 1
δ_{dr}	Detuning of ω_{dr} from the shifted $ D\rangle$ and $ F\rangle$ state energy gap
S_δ	Scaling parameter for δ_{dr} , near 1.0
ε_N	N^{th} Floquet sideband quasi-energy
$(\cdot)_\pm$	Two values represented, for the upper (+) and lower (−) AT dressed state

TABLE I. Table of non-standard variables used in this paper.